PHYSICAL REVIEW B **89**, 241401(R) (2014)

Finite-size versus interface-proximity effects in thin-film epitaxial $SrTiO_3$

R. A. De Souza,[1,*] F. Gunkel,[2] S. Hoffmann-Eifert,[2] and R. Dittmann[2]

[1]*Institute of Physical Chemistry, RWTH Aachen University and JARA-FIT, 52056 Aachen, Germany*

[2]*Peter Grünberg Institut, Forschungszentrum Jülich GmbH and JARA-FIT, 52425 Jülich, Germany*

(Received 27 September 2013; revised manuscript received 4 April 2014; published 4 June 2014)

The equilibrium electrical conductivity of epitaxial $SrTiO_3$ (STO) thin films was investigated as a function of temperature, $950 \leqslant T/\mathrm{K} \leqslant 1100$, and oxygen partial pressure, $10^{-23} \leqslant pO_2/\mathrm{bar} \leqslant 1$. Compared with single-crystal STO, nanoscale thin-film STO exhibited with decreasing film thickness an increasingly enhanced electronic conductivity under highly reducing conditions, with a corresponding decrease in the activation enthalpy of conduction. This implies substantial modification of STO's point-defect thermodynamics for nanoscale film thicknesses. We argue, however, against such a finite-size effect and for an interface-proximity effect. Indeed, assuming trapping of oxygen vacancies at the STO surface and concomitant depletion of oxygen vacancies—and accumulation of electrons—in an equilibrium surface space-charge layer, we are able to predict quantitatively the conductivity as a function of temperature, oxygen partial pressure, and film thickness. Particularly complex behavior is predicted for ultrathin films that are consumed entirely by space charge.

DOI: 10.1103/PhysRevB.89.241401 PACS number(s): 73.63.−b, 68.35.Dv, 73.30.+y

Increasingly, transition-metal oxides are coming under consideration for the key components in conventional and novel electronic devices [1–5]. The perovskite oxides—$SrTiO_3$ (STO) and $BaTiO_3$ (BTO), for example—have been suggested for use, in the form of thin films, as the high-k dielectric in standard semiconductor technology [6], as the tunnel barrier in multiferroic tunnel junctions [7], and as the active layer in memristive elements [8].

Understanding and controlling charge-carrier densities in these oxide thin films is critical to their successful application. For example, the use of STO [9] or the related ferroelectric oxide BTO [10] as the tunnel barrier in multiferroic tunnel junctions requires current transport to occur by charge-carrier injection from the electrodes: charge carriers originating from the tunnel barrier itself are undesired. Such parasitic charge carriers, evidenced by the high leakage currents observed for ultrathin STO [11] and BTO [12,13] films, have often been suspected to be caused by a high density of ionic defects, predominantly oxygen vacancies, induced during thin-film growth [14]. In general, charge-carrier densities in thin films appear to differ significantly from those in single crystals.

In this Rapid Communication we investigate the high-temperature, equilibrium conductivity of epitaxial STO thin films as a function of temperature T and oxygen partial pressure pO_2. Since the measurements refer to thermodynamic equilibrium between the sample and the surrounding gas phase, excess oxygen vacancies produced during growth are absent from the sample, although they are of course readily generated or annihilated through equilibration with the ambient atmosphere; and they are formed to compensate acceptorlike impurities (self-compensation). In any case, the measured conductivity is dictated by equilibrium thermodynamic processes. We find that the experimentally measured conductivity varies strongly with film thickness. We then discuss whether the point-defect thermodynamics are altered at the nanoscale (a finite-size effect), or whether space-charge layers become increasingly important at the nanoscale (an interface-proximity effect). Both explanations have been applied, albeit qualitatively, to nanoscale STO and BTO systems [15–19]. Here we demonstrate that an interface-proximity effect explains quantitatively the observed behavior, and we draw attention to the consequences.

Heteroepitaxial STO thin films were grown on (001) $(La_{0.3}Sr_{0.7})(Al_{0.65}Ta_{0.35})O_3$ (LSAT) substrates by pulsed laser deposition (PLD) from a single-crystal target of nominally undoped STO. PLD conditions were optimized to ensure growth of stoichiometric STO [20–22]. STO thin films were deposited with layer thicknesses of (a) $d = 3.9$ nm [10 unit cells (10 uc), $a_{STO} = 0.39$ nm] and (b) $d = 160$ nm. Further details of sample deposition and characterization are given as Supplemental Material [23]. Four Pt contacts were sputtered onto a sample for the *in situ*, four-point, dc conductance measurements. These were performed with an in-house system based on an yttria-stabilized zirconia oxygen pump [15]. After a change in oxygen partial pressure or temperature, the conductance Y of the sample was monitored until no further change was observed: In this way we can be confident that thermodynamic equilibrium was established between the sample and the surrounding atmosphere, and hence that the measured conductance is the high-temperature equilibrium conductance (HTEC).

We chose LSAT as a substrate for two reasons. First, the small, temperature-independent lattice mismatch between STO and LSAT allows growth of high-quality, epitaxial STO thin films, with a small compressive strain of $(a_{LSAT} - a_{STO})/a_{STO} \approx -0.9\%$. Second, the HTEC of LSAT is low, even at elevated temperatures [24]. Nevertheless, comparing the measured HTEC of the 10-uc-thick STO layer on LSAT with that of a bare (reference) LSAT substrate (see Fig. S4 [23]), we find that only under highly reducing conditions, $pO_2 < 10^{-14}$ bar, can the conductance be unambiguously assigned to the 10 uc STO thin film; at higher oxygen partial pressures the LSAT substrate dominates. The analysis and discussion of experimental data is confined, therefore, to the HTEC of thin-film STO under highly reducing conditions.

*desouza@pc.rwth-aachen.de

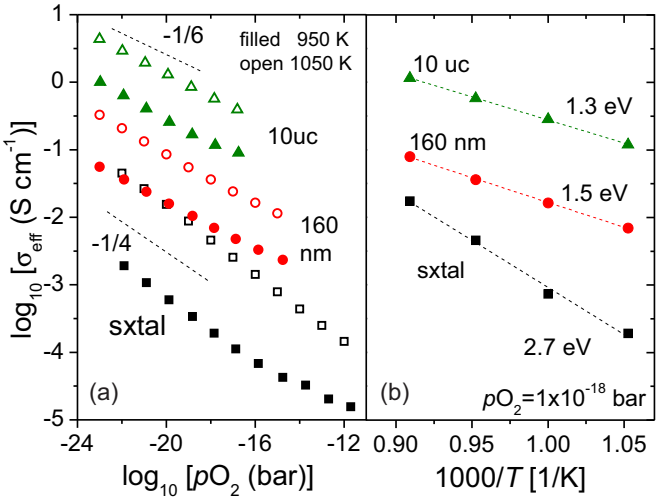

FIG. 1. (Color online) Effective conductivity of heteroepitaxial thin-film STO compared with that of single-crystal STO: (a) as a function of oxygen partial pressure and (b) as a function of temperature. The thin-film data is limited to highly reducing conditions, for which the conductance of the thin film dominates the conductance of the film|substrate sample.

In Fig. 1 we plot for two selected temperatures the effective conductivity of the two investigated film thicknesses (10 uc and 160 nm), and for comparison, the conductivity measured for an undoped single-crystal STO sample (sxtal). Note, for the chosen measurement geometry, $\sigma_{\text{eff}} = Y/d$, see Fig. S4(a) [23]. Starting with single-crystal STO, we find that the data agree exceptionally well with literature data [15,25–28], not only in terms of the absolute magnitude but also in terms of the activation enthalpy of the conductivity, $\Delta H_{\sigma}^{\text{sxtal}} = (2.7 \pm 0.1)$ eV, and the dependence on oxygen partial pressure, $\sigma_{\text{eff}}^{\text{sxtal}} \propto (pO_2)^{-1/4}$. Moving on to the 160-nm-thick STO film, we find that the effective conductivity is ca. one order of magnitude higher than that of the single crystal, and that this enhancement is accompanied by a strong decrease in activation enthalpy, $\Delta H_{\sigma}^{160\text{ nm}} = (1.5 \pm 0.1)$ eV, and by a substantial weakening of the the pO_2 dependence, $\sigma_{\text{eff}}^{160\text{ nm}} \propto (pO_2)^{-1/5.5}$. For the third system, the 10 uc film, the changes are amplified: The conductivity is increased further, being two to three orders of magnitude higher than the bulk conductivity; the activation enthalpy is decreased further, $\Delta H_{\sigma}^{10\text{ uc}} = (1.3 \pm 0.1)$ eV; and the pO_2 dependence is weakened further, $\sigma_{\text{eff}}^{10\text{ uc}} \propto (pO_2)^{-1/6}$. Thus on traversing the samples from single crystal, via 160 nm thin film, to 10 uc thin film, we find a monotonic increase in conductivity, a monotonic decrease in activation enthalpy, and a monotonic weakening of the pO_2 dependence.

The characteristic exponent of $-1/4$ obtained for the single crystal in this pO_2 range, $\sigma_{\text{eff}}^{\text{sxtal}} \propto (pO_2)^{-1/4}$, indicates importantly that (i) the conductivity is n-type, the electrons being generated by the reduction of STO according to (with oxygen vacancies being fully ionized, $V_O^{\cdot\cdot}$, at the conditions of the HTEC measurements [26])

$$O_O^{\times} \rightleftharpoons V_O^{\cdot\cdot} + 2e' + \tfrac{1}{2}O_2; \qquad (1)$$

and (ii) that the nominally undoped STO single crystal is in fact weakly acceptor doped (from unintentionally included impurities) [15,26,29].

Given that the n-type electronic conductivity can be expressed as the product of the electrons' concentration, charge, and mobility ($\sigma_n = ne\mu_n$), the enhancements observed for the nanoscale films could be due to modification of the electron concentration n or of the electron mobility μ_n, or a combination of both. At the high temperatures of our HTEC measurements, phonon scattering governs the mobility [25,26,30–32], and this is unlikely to differ significantly between single crystals and thin films. The observed enhancement in σ_{eff} evidently arises, therefore, from an increase in n.

The obvious explanation for this increase is that the point-defect thermodynamics of STO are size dependent. To be specific, ΔH_{red}, the enthalpy of the reduction reaction [Eq. (1)], is required to decrease with decreasing film thickness. Such a decrease in ΔH_{red} would explain the enhancement of σ_{eff}, the decrease in ΔH_{σ}, and the weakening of the pO_2 dependence (Fig. 1). Though simple, this explanation is unsatisfactory for two reasons. First, although there are many examples of solids exhibiting size-dependent thermodynamic properties [33], they all refer to cases in which a significant proportion of the constituent atomic species is situated close to an interface, i.e., the characteristic extent of the system is a few nanometers. Thus, the 10 uc film is expected to behave differently to the bulk single crystal (and does), but the 160 nm film should display bulklike behavior (and does not). Indeed, the conductivity of the 160 nm film is closer in behavior to that of the 10 uc film than to that of the bulk single crystal. Second, in appealing to this explanation one implicitly assumes local charge neutrality, but this is not necessarily the case. In the vicinity of an interface, local charge neutrality is often violated: A space-charge layer is present, in which the concentrations of mobile charge carriers are drastically modified from their bulk values. Below we show that electron accumulation in a surface space-charge layer—an interface-proximity effect—can explain quantitatively, within a single model, the behavior of both film thicknesses.

In our model, nonuniform charge-carrier distributions across the films are governed by the behavior of the oxygen vacancies. Specifically, an equilibrium surface space-charge layer is formed as a result of fully ionized oxygen vacancies having a lower Gibbs energy of formation at the surface than in the bulk, $\Delta g_{\{V_O^{\cdot\cdot}\}} = g_{\{V_O^{\cdot\cdot}\}}^{s} - g_{\{V_O^{\cdot\cdot}\}}^{b} < 0$ [29,34]; essentially, $\Delta g_{\{V_O^{\cdot\cdot}\}}$ is the Gibbs energy for the trapping of oxygen vacancies at the surface. (The surface is defined here as the uppermost, half unit-cell layer; its extent is thus $w_s = a_{\text{STO}}/2$.) By redistributing oxygen vacancies to the surface from the bulk phase, electrostatically charging the surface and the adjacent bulk phase in the process, the system can lower its Gibbs energy from the initially homogeneous, locally neutral state: In this sense a surface can be considered as "half a grain boundary" [34–36]. The electrical potential $\phi(x)$ associated with this charging causes electron accumulation in the surface space-charge zone (see Fig. 2), and it is this region of excess electrons that is responsible for the enhanced conductivity of the thin films. In a band diagram [Fig. 2(c)], the conduction band (CB) and valence band (VB) bend

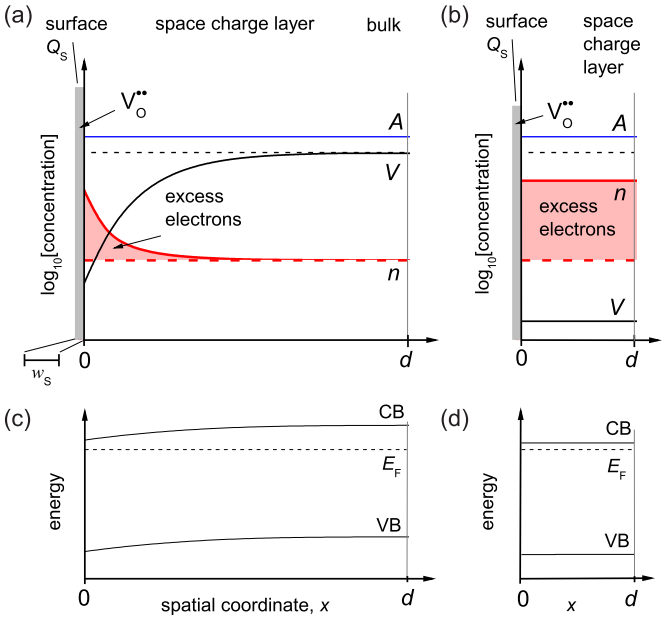

FIG. 2. (Color online) Schematic diagrams of point-defect concentrations [(a),(b)] and of the corresponding energy levels [(c),(d)] for STO under highly reducing conditions for two extreme cases: semi-infinite case, $d > \lambda^*$ [(a),(c)]; flat-band case, $d \ll \lambda^*$ [(b),(d)]. Redistribution of oxygen vacancies from bulk to surface (gray bar) generates an electrical potential that causes electrons to accumulate close to the interface. In (a) and (b), A (blue), V (black), and n (red) are the concentrations of acceptors, oxygen vacancies, and electrons, respectively; dashed lines indicate bulk values.

downwards in the near-surface region, so that the Fermi energy E_F approaches the CB edge. Note, as shown in Figs. 2(a) and 2(b), the positively charged vacancies at the surface are compensated in the adjacent bulk phase primarily by the now uncompensated acceptor-dopant cations and partly by the accumulated electrons; the latter contribute more to the compensating charge as the conditions become more reducing.

The measured conductance in the plane of the thin film is the sum of the bulk conductance Y^b and the excess conductance from the space-charge layer ΔY_{sc} (i.e., the shaded area in Fig. 2 multiplied by $\mu_n e$); the effective conductivity follows as

$$\sigma_{\text{eff}} = \sigma_n^b + \frac{\Delta Y_{sc}}{d} = \mu_n e\left(n^b + \frac{\int_0^d [n(x) - n^b]dx}{d}\right). \quad (2)$$

In order to obtain $n(x)$ and hence ΔY_{sc}, we solved three coupled equations in an iterative, self-consistent procedure for each pO_2, T, and d:

(1) In an equilibrium space-charge zone, the electrochemical potentials of all mobile charge carriers are constant throughout the system. Assuming the standard form for the electrochemical potential of the point-defect building unit [34,37] in the bulk phase (^{b}) and at the surface (^{s}), one can write for each of the three mobile species (electrons, electron holes, and oxygen vacancies)

$$k_B T \ln \frac{c_{\text{def}}^s}{N_{\text{def}}^s - c_{\text{def}}^s} - k_B T \ln \frac{c_{\text{def}}^b}{N_{\text{def}}^b - c_{\text{def}}^b} + \Delta g_{\{\text{def}\}} + z_{\text{def}} e \Phi_0 = 0, \quad (3)$$

to link the thermodynamic driving energies $\Delta g_{\{\text{def}\}}$ to the space-charge potential Φ_0. c_{def}, N_{def}, and z_{def} are the concentration, density of available sites, and charge number of the charge carrier "def." For electrons and holes, N_{def} is the effective density of states at the conduction-band and valence-band edges, respectively. $\Delta g_{\{\text{def}\}}$ for electrons and holes are the conduction-band and valence-band offsets between surface and bulk phases.

(2) The electrical potential in the space-charge layer $\phi(x)$ is given by the solution to the one-dimensional Poisson equation ($\epsilon_r\epsilon_0$ is the dielectric permittivity)

$$\epsilon_r\epsilon_0 \frac{d^2\phi}{dx^2} = -e\left[A - \sum \frac{z_{\text{def}} N_{\text{def}}^b c_{\text{def}}^b e^{-z_{\text{def}} e\phi/k_B T}}{N_{\text{def}}^b + c_{\text{def}}^b (e^{-z_{\text{def}} e\phi/k_B T} - 1)}\right] \quad (4)$$

for the boundary conditions $\Phi_0 = \phi(0) - \phi(\infty)$ and $\nabla\phi(d) = 0$. The second boundary condition approximates the heteroepitaxial film as one active (gas|STO) interface and one inactive (STO|LSAT) interface. The alternative approximation of $\nabla\phi(d/2) = 0$, i.e., two active surfaces, does not change the results qualitatively. Acceptor impurities are assumed to be immobile; their concentration A is thus constant across the film.

(3) The thin film as a whole is electrically neutral, i.e., the space charge is compensated exactly by the charge of the surface, $Q_{sc} + Q_s = 0$, or

$$\epsilon_r\epsilon_0 \left.\frac{d\phi}{dx}\right|_{x=0} + w_s \sum z_{\text{def}} e\left(c_{\text{def}}^s - c_{\text{def}}^b\right) = 0. \quad (5)$$

We stress that Φ_0 and Q_s may vary with d, T, pO_2, and A because the values they take are dictated by Eqs. (3)–(5), with the boundary condition $\nabla\phi(d) = 0$. In contrast, $\Delta g_{\{V_O^{\bullet\bullet}\}}$ is independent of these variables, being specific to the material (STO) and the interface [(100) surface].

In order to obtain σ_{eff}, one has to specify point-defect concentrations in the bulk, $c_{\text{def}}^b(T, pO_2)$, resulting from $A \approx 10^{18}$ cm^{-3} (see Fig. S5 [23]); the electron mobility $\mu_n(T)$ [26]; and the dielectric permittivity, which only depends on temperature not electric field in the studied temperature range, $\epsilon_r(T)$ [38]. Furthermore, we assumed for the surface: N_{def}^s to be equal to N_{def}^b; and $\Delta g_{\{\text{def}\}}$ to be zero for electrons and electron holes. The sole driving energy is thus $\Delta g_{\{V_O^{\bullet\bullet}\}} = -1.4$ eV (a value determined experimentally [29]). The entire computational procedure was implemented in MATLAB (The Mathworks, Inc.).

In Fig. 3 we compare the calculated values of σ_{eff} with the experimental results. Three aspects need to be emphasized: Not only is the increase in σ_{eff} with decreasing film thickness reproduced, but also the weakening of the pO_2 dependence [$\sigma \propto (pO_2)^{-1/m_\sigma}$], m_σ^{calc}(sxtal : 160 nm : 10 uc) = 4.0 : 4.7 : 5.8, and the decrease in activation enthalpy of conduction, $\Delta H_\sigma^{\text{calc}}$(sxtal : 160 nm : 10 uc) [eV] = 2.6 : 1.5 : 1.3. Detailed analysis reveals that the changes are due to the combination of Φ_0 varying with pO_2, T, and d, and of the space-charge layer becoming increasingly important with decreasing film thickness. The calculations do overestimate $\sigma_{\text{eff}}^{10\text{ uc}}$. And it is not clear whether this is due to the use of a continuum approach for such a small (10 uc) system; to experimental inaccuracy; or to a real effect. The compressive strain observed for this ultrathin film may conceivably cause an increase in ΔH_{red},

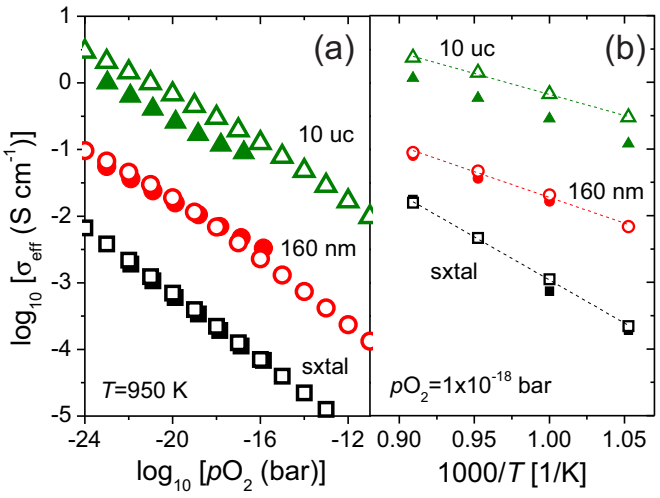

FIG. 3. (Color online) Comparison of experimental data (closed symbols) and theoretical predictions from the space-charge model (open symbols): (a) as a function of oxygen partial pressure; (b) as a function of temperature.

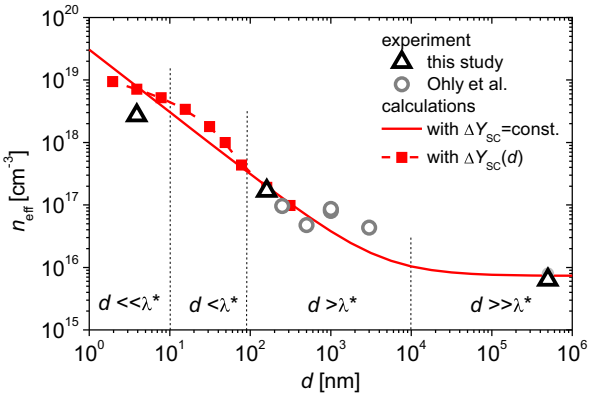

FIG. 4. (Color online) Variation with sample thickness d of the effective electron concentration $n_{\rm eff}$ in STO at high temperature (T = 950 K) and highly reducing conditions ($pO_2 = 10^{-20}$ bar). Space-charge screening length, $\lambda^* = 90$ nm for this T and A.

and thus a decrease in $n^{\rm b}$. If real, this would be a secondary interface-proximity effect.

(Incidentally, cation intermixing across the STO|LSAT interface appears to be insignificant. As a primary effect, it is unable to account for the enhanced conductivity of either film thickness as a function of T *and* pO_2. As a secondary effect it cannot explain why the measured $\sigma_{\rm eff}^{10\ {\rm uc}}$ is lower than the calculated value.)

One point not apparent in Fig. 3 is the rich behavior of $\sigma_{\rm eff}$ as a function of film thickness d, especially for $d \leqslant \lambda^*$, where $\lambda^* = \sqrt{2\epsilon_0\epsilon_{\rm r}\Phi_0/eA}$ is the space-charge screening length for the case of immobile acceptors. To this end we consider in Fig. 4 the effective electron concentration $n_{\rm eff} = \sigma_{\rm eff}/\mu_n e$ as a function of d. The solid line was calculated for all d from the single, semi-infinite value of $\Delta Y_{\rm sc}$ [see Fig. 2(b), in which $\phi(x)$ decays from Φ_0 at the surface to zero *before* the end of the film is reached]. The square symbols refer to values of $\Delta Y_{\rm sc}$ calculated individually for a specific value of d. For films with $d > \lambda^*$, the two are identical (as expected), but as d decreases below λ^*, differences appear. They arise because $\phi(d) \neq 0$, i.e., the entire film is consumed by space charge and defect concentrations do not attain their bulk values anywhere in the film. This is a finite-size effect, though secondary to the (primary) interface-proximity effect. For ultrathin films ($d \ll \lambda^*$), $\phi(0)/\phi(d)$ approaches unity (flat-band case) [Fig. 2(d)]. Differences have been previously predicted for $d < \lambda^*$ [39], but the behavior predicted here—an initial, modest enhancement, and thereafter, a plateau as the flat-band case is attained—is far more complex than literature considerations [39,40] because in our case, Φ_0 is not assumed to be constant but may vary with d, as a consequence of specifying the thermodynamic driving energies $\Delta g_{\{\rm def\}}$.

Also plotted in Fig. 4 are experimental data extracted from this study and from an earlier study on thicker films [15]. These data agree well with the theoretical predictions. The plot also emphasizes that the 160 nm film corresponds to $d > \lambda^*$, with $\phi(160\ {\rm nm}) = 0$ [cf. Fig. 2(c)], whereas the 10 uc film corresponds to the flat-band case, with $\phi(0)/\phi(d) \approx 1$ [cf. Fig. 2(d)]. On going to higher oxygen partial pressures, the entire graph shifts to lower $n_{\rm eff}$. Nevertheless, for ultrathin films we predict that, even after annealing at $pO_2 = 1$ bar, such samples will display n-type conductivity, with $n_{\rm eff} \approx 10^{14}\ {\rm cm}^{-3}$. Furthermore, upon quenching to room temperature, $n_{\rm eff}$ will not depart from the high-temperature values considerably. Thus ultrathin-film STO will always display an enhanced concentration of electrons relative to single-crystal STO: It is unavoidable because electron accumulation in the surface space-charge layer is an equilibrium phenomenon. Only through judicious choice of electrodes, thereby modifying $\Delta g_{\{\rm def\}}$, may the effects be alleviated.

Lastly we note that our results apply to acceptor-doped and nominally undoped (=acceptor-doped by impurities) systems. Donor-doped thin films are characterized by surface depletion of electrons [41,42] instead of accumulation, possibly due to oxidation of the surface [43].

In summary we conclude that an equilibrium space-charge layer at the STO surface accounts for the films' enhanced n-type conductivity σ_n, lowered activation enthalpy ΔH_σ, and weaker pO_2 dependence. The primary effect is thus an interface-proximity effect, although additional complexities are generated by secondary finite-size (and possibly interface-proximity) effects. The inhomogeneous, equilibrium distribution of oxygen vacancies (and other charge carriers) across a thin film is expected to be characteristic of perovskite oxides, in particular, and other oxides, in general.

We acknowledge funding from the German Science Foundation (DFG) within the collaborative research center, SFB 917 "Nanoswitches." We thank R. Waser (RWTH Aachen and FZ Jülich) for valuable comments.

[1] J. Mannhart and D. G. Schlom, Science **327**, 1607 (2010).
[2] H. Takagi and H. Y. Hwang, Science **327**, 1601 (2010).
[3] R. Waser, R. Dittmann, G. Staikov, and K. Szot, Adv. Mater. **21**, 2632 (2009).

[4] M. Bibes, J. E. Villegas, and A. Barthélémy, Adv. Phys. **60**, 5 (2011).
[5] S. V. Kalinin and N. A. Spaldin, Science **341**, 858 (2013).
[6] A. I. Kingon, J.-P. Maria, and S. K. Streiffer, Nature (London) **406**, 1032 (2000).
[7] E. Y. Tsymbal and H. Kohlstedt, Science **313**, 181 (2006).
[8] K. Szot, R. Dittmann, W. Speier, and R. Waser, Phys. Status Solidi RRL **1**, R86 (2007).
[9] M. Bowen, M. Bibes, A. Barthélémy, J.-P. Contour, A. Anane, Y. Lemaître, and A. Fert, Appl. Phys. Lett. **82**, 233 (2003).
[10] V. Garcia, S. Fusil, K. Bouzehouane, S. Enouz-Vedrenne, N. D. Mathur, A. Barthélémy, and M. Bibes, Nature (London) **460**, 81 (2009).
[11] W. Hofman, S. Hoffmann, and R. Waser, Thin Solid Films **305**, 66 (1997).
[12] Y. S. Kim, D. H. Kim, J. D. Kim, Y. J. Chang, T. W. Noh, J. H. Kong, K. Char, Y. D. Park, S. D. Bu, J.-G. Yoon, and J.-S. Chung, Appl. Phys. Lett. **86**, 102907 (2005).
[13] A. Petraru, H. Kohlstedt, U. Poppe, R. Waser, A. Solbach, U. Klemradt, J. Schubert, W. Zander, and N. A. Pertsev, Appl. Phys. Lett. **93**, 072902 (2008).
[14] M. L. Scullin, J. Ravichandran, C. Yu, M. Huijben, J. Seidel, A. Majumdar, and R. Ramesh, Acta Mater. **58**, 457 (2010).
[15] C. Ohly, S. Hoffmann-Eifert, X. Guo, J. Schubert, and R. Waser, J. Am. Ceram. Soc. **89**, 2845 (2006).
[16] P. Balaya, J. Jamnik, J. Fleig, and J. Maier, J. Electrochem. Soc. **154**, P69 (2007).
[17] X. Guo, C. Pithan, C. Ohly, C.-L. Jia, J. Dornseiffer, F.-H. Haegel, and R. Waser, Appl. Phys. Lett. **86**, 082110 (2005).
[18] P. Lupetin, G. Gregori, and J. Maier, Angew. Chem. **122**, 10321 (2010).
[19] X. Guo, Acta Mater. **61**, 1748 (2013).
[20] T. Ohnishi, K. Shibuya, T. Yamamoto, and M. Lippmaa, J. Appl. Phys. **103**, 103703 (2008).
[21] J. M. LeBeau, R. Engel-Herbert, B. Jalan, J. Cagnon, P. Moetakef, S. Stemmer, and G. B. Stephenson, Appl. Phys. Lett. **95**, 142905 (2009).
[22] D. J. Keeble, S. Wicklein, R. Dittmann, L. Ravelli, R. A. Mackie, and W. Egger, Phys. Rev. Lett. **105**, 226102 (2010).
[23] See Supplemental Material at http://link.aps.org/supplemental/10.1103/PhysRevB.89.241401 for PLD, AFM, reflection high-energy electron diffraction, defect chemistry.
[24] F. Gunkel, P. Brinks, S. Hoffmann-Eifert, R. Dittmann, M. Huijben, J. E. Kleibeuker, G. Koster, G. Rijnders, and R. Waser, Appl. Phys. Lett. **100**, 052103 (2012).
[25] G. M. Choi and H. L. Tuller, J. Am. Ceram. Soc. **71**, 201 (1988).
[26] R. Moos and K. H. Härdtl, J. Am. Ceram. Soc. **80**, 2549 (1997).
[27] R. Waser, J. Am. Ceram. Soc. **74**, 1934 (1991).
[28] F. Gunkel, S. Hoffmann-Eifert, R. Dittmann, S. B. Mi, C. L. Jia, P. Meuffels, and R. Waser, Appl. Phys. Lett. **97**, 012103 (2010).
[29] R. A. De Souza, V. Metlenko, D. Park, and T. E. Weirich, Phys. Rev. B **85**, 174109 (2012).
[30] H. P. R. Frederikse and W. R. Hosler, Phys. Rev. **161**, 822 (1967).
[31] O. N. Tufte and P. W. Chapman, Phys. Rev. **155**, 796 (1967).
[32] J. Son, P. Moetakef, B. Jalan, O. Bierwagen, N. J. Wright, R. Engel-Herbert, and S. Stemmer, Nat. Mater. **9**, 482 (2010).
[33] A. Navrotsky, ChemPhysChem **12**, 2207 (2011).
[34] R. A. De Souza, Phys. Chem. Chem. Phys. **11**, 9939 (2009).
[35] R. Waser and R. Hagenbeck, Acta Mater. **48**, 797 (2000).
[36] P. C. McIntyre, J. Am. Ceram. Soc. **83**, 1129 (2000).
[37] D. R. Franceschetti, Solid State Ionics **2**, 39 (1981).
[38] J. Maier, G. Schwitzgebel, and H.-J. Hagemann, J. Solid State Chem. **58**, 1 (1985).
[39] J. Maier, Prog. Solid State Chem. **23**, 171 (1995).
[40] J. Jamnik, Solid State Ionics **177**, 2543 (2006).
[41] A. Ohtomo and H. Y. Hwang, Appl. Phys. Lett. **84**, 1716 (2004).
[42] M. Kim, C. Bell, Y. Kozuka, M. Kurita, Y. Hikita, and H. Y. Hwang, Phys. Rev. Lett. **107**, 106801 (2011).
[43] R. Meyer, R. Waser, J. Helmbold, and G. Borchardt, Phys. Rev. Lett. **90**, 105901 (2003).